The Compact Muon Solenoid Experiment
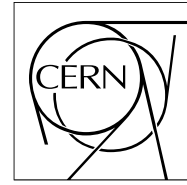
CMS Note

Mailing address: CMS CERN, CH-1211 GENEVA 23, Switzerland

Beam Test Performance of Prototype Silicon Detectors for the Outer Tracker for the Phase-2 Upgrade of CMS

Jeremy Andrea[4], Panagiotis Assiouras[8], Georg Auzinger[12], Rajarshi Bhattacharya[9], Anadi Canepa[14], Nicolas Pierre Chanon[5], Vladimir Cherepanov[4], Nikkie Deelen[11], Martin Delcourt[1], Alexander Dierlamm[6], Suchandra Dutta[9], Thomas Eichhorn[7], Tomasz Gadek[11], Yuri Gershtein[15], Geoffrey Hall[12], Mykyta Haranko[7], Robert Harr[16], Siew Yan Hoh[14], Alan Honma[11], Tom James[12], Mark Kovacs[11], Aristoteles Kyriakis[8], Dimitrios Loukas[8], Jelena Luetic[3], Stefano Mersi[11], Mark Pesaresi[12], Nabin Poudyal[16], Alan Prosser[14], Ryan Rivera[14], Alessandro Rossi[10], Suvankar Roy Chowdhury[9], Subir Sarkar[9], Basil Schneider[14], Sarah Seif El Nasr[13], Jarne Theo De Clercq[2], Kirika Uchida[12], Lorenzo Uplegger[14], and Giovanni Zevi Della Porta[17]

[1]Université Catholique de Louvain, Louvain-la-Neuve, Belgium
[2]Vrije Universiteit Brussel, Brussel, Belgium
[3]Université Libre de Bruxelles, Bruxelles, Belgium
[4]Université de Strasbourg, CNRS, IPHC UMR 7178, Strasbourg, France
[5]Université de Lyon, Université Claude Bernard Lyon 1, CNRS-IN2P3, Institut de Physique Nucléaire de Lyon, Villeurbanne, France
[6]Institut für Experimentelle Teilchenphysik, Karlsruhe, Germany
[7]Deutsches Elektronen-Synchrotron, Hamburg, Germany
[8]Institute of Nuclear and Particle Physics (INPP), NCSR Demokritos, Aghia Paraskevi, Greece
[9]Saha Institute of Nuclear Physics, HBNI, Kolkata, India
[10]INFN Sezione di Perugia, Università di Perugia, Perugia, Italy
[11]CERN, European Organization for Nuclear Research, Geneva, Switzerland
[12]Imperial College, London, United Kingdom
[13]University of Bristol, Bristol, United Kingdom
[14]Fermi National Accelerator Laboratory, Batavia, USA
[15]Rutgers, The State University of New Jersey, Piscataway, USA
[16]Wayne State University, USA
[17]University of California, San Diego, La Jolla, USA

Abstract

A new CMS tracker detector will be installed for operation at the High Luminosity LHC (HL-LHC). This detector comprises modules with two closely spaced parallel sensor plates and front-end ASICs capable of transmitting tracking information to the CMS Level-1 (L1) trigger at the 40 MHz beam crossing rate. The inclusion of tracking information in the L1 trigger decision will be essential for selecting events of interest efficiently at the HL-LHC. The CMS Binary Chip (CBC) has been designed to read out and correlate hits from pairs of tracker sensors, forming so-called track stubs. For the first time, a prototype irradiated module and a full-sized module, both equipped with the version 2 of the CBC, have been operated in test beam facilities. The efficiency of the stub finding logic of the modules for various angles of incidence has been studied. The ability of the modules to reject tracks with transverse momentum less than 2 GeV has been demonstrated. For modules built with irradiated sensors, no significant drop in the stub finding performance has been observed. Results from the beam tests are described in this paper.

1 Introduction

The Large Hadron Collider (LHC) at CERN will undergo major upgrades by 2025 to be able to deliver peak instantaneous luminosities of $5 - 7.5 \times 10^{34} \text{cm}^{-2}\text{s}^{-1}$. This High Luminosity upgrade of the LHC (HL-LHC) will allow the CMS (Compact Muon Solenoid) [1] experiment to collect data corresponding to integrated luminosities of the order of 300 fb^{-1} per year. Eventually, a total of 3000 fb^{-1} will be collected during ten years of operation. At the nominal instantaneous luminosity of the HL-LHC, a single bunch crossing will produce 140-200 proton-proton collisions. The vast majority of these collisions are "pileup" interactions with low momentum transfer that are of little physics interest.

In order to fully exploit the increased luminosity and to cope with the very high pileup environment, the detector and the trigger system of the CMS experiment need to be upgraded significantly [2]. The present CMS tracker was designed to operate up to an integrated luminosity of 500 fb^{-1} [2, 3], beyond which radiation damage will lead to degradation of its performance. The CMS experiment will replace the current tracker with a new silicon tracker. The upgraded tracker [3] will feature increased radiation hardness, higher granularity, compatibility with higher data rates, and a longer trigger latency. In addition, the tracker will provide tracking information to the Level-1 trigger, allowing trigger rates to be kept at a sustainable level without sacrificing physics potential [3].

The CMS tracker for the HL-LHC period will consist of modules with two "stacked" silicon sensors, read out by front-end ASICs with the capability to discriminate tracks based on their transverse momentum (p_T). The concept of p_T discrimination by means of very short track segments called stubs, in so-called p_T modules, will be discussed in the following section.

A number of module prototypes described in the following section, each with two stacked strip sensors, also known as 2S modules, were subjected to particle beams at CERN, Fermilab, and DESY beam test facilities to measure the performance of the stub finding mechanism, the uniformity of the stub finding efficiency in the entire detector, the potential to reject low p_T tracks (< 2 GeV), and the ability to work efficiently up to the expected overall HL-LHC radiation level. In this paper, results from beam tests carried out at CERN are reported and, where possible, compared to those obtained at Fermilab and DESY. The results from previous beam test are reported in Ref. [4].

2 CMS Tracker for HL-LHC

The layout of the new tracker is shown in Fig. 1. The new tracker will consist of two parts: an Inner Tracker (IT) and an Outer Tracker (OT). Both the IT and the OT will have a barrel section, made out of coaxial cylindrical layers, and two endcaps, one on each side of the barrel, made out of discs. The IT barrel will feature four layers of pixel detectors, providing three-dimensional hit coordinates, resulting in excellent vertex resolution. Each IT endcap will consist of 12 pixel discs on each side of the barrel. The OT barrel will comprise six layers of detector modules each having two silicon sensors separated by a small distance and read out by the same front-end electronics. The separation between the sensors of a module, defined by the distance between the sensor mid planes, will vary between 1.6 mm and 4 mm [3]. Of the six layers of the OT barrel, the three inner layers will be equipped with modules made of one macro-pixel sensor and one strip sensor (PS p_T module). The three outer layers will be equipped with modules with two strip sensors (2S p_T module). The OT endcaps will feature six discs and will be equipped with PS and 2S modules, as shown in Fig. 1. The main specifications of the PS and 2S modules for the OT are listed in Table 1.
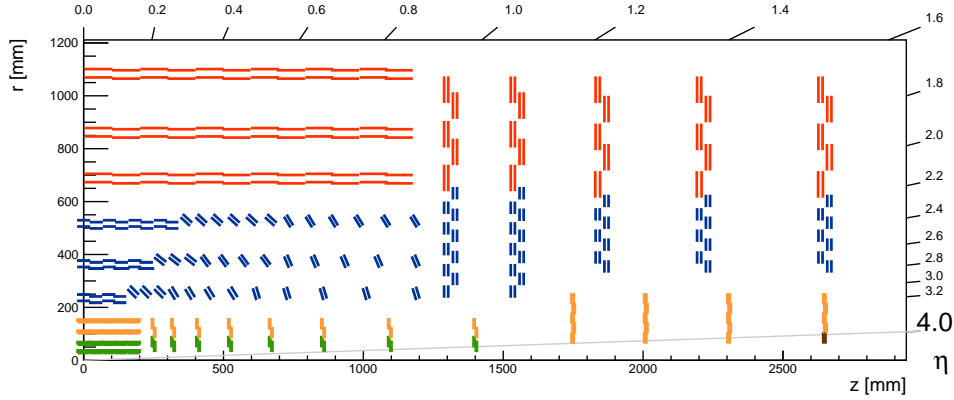
Figure 1: Sketch of one quarter of the tracker layout in r − z view. The radial region below 200 mm is referred to as Inner Tracker and will be instrumented with pixel modules. In the Outer Tracker, the radial region between 200 and 600 mm is equipped with PS modules (blue lines), while the region beyond 600 mm will be populated with 2S modules (red lines). The CMS coordinate system is defined in Ref. [1].

Table 1: Main parameters of the 2S and PS modules of the proposed CMS Phase-2 tracker [3].

2S module			PS module		
$\sim 2 \times 90$ cm^2 active area			$\sim 2 \times 45$ cm^2 active area		
No. of strips/sensor plane	Strip length	Pitch	No. of strips/macro-pixels	Strip/macro-pixel length	Pitch
2×1016	~ 5 cm	90 μm	$2 \times 960/32 \times 960$	~ 2.4 cm/~ 1.5 mm	100 μm

2.1 The Concept of p_T Discrimination

In the presence of the 3.8 T solenoidal magnetic field inside the CMS detector, the trajectories of charged particles produced in a collision will bend in a plane transverse to the direction of the beam. The radius of the curvature of the trajectory of these particles depends on the particle p_T. The concept of p_T discrimination is shown in Fig. 2. As a charged particle passes through the module, it generates signals (hits) in the bottom and top sensors of the module. A hit in the bottom sensor is then matched to the one in the top sensor and if they are within a predefined window, these two hits are combined to form a short track segment or stub. These stubs will be used in the Level-1 (L1) track trigger.
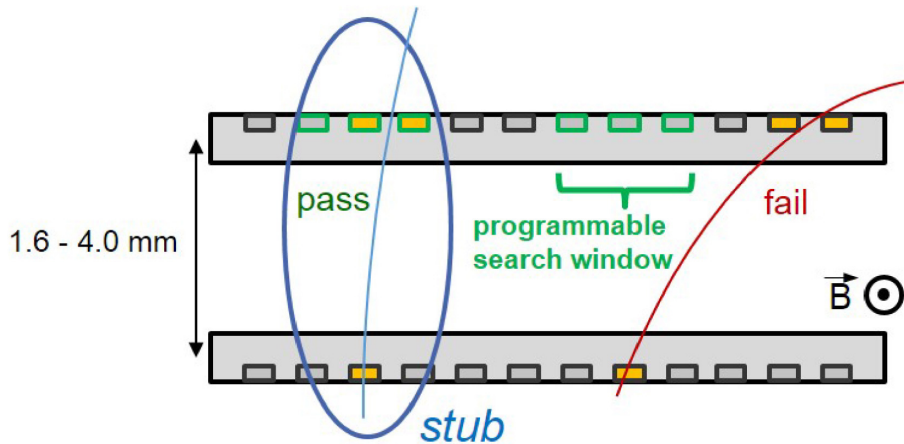

Figure 2: Illustration of the p_T module concept [3]. Correlation of signals in closely spaced sensors enables rejection of low-p_T particles. The channels shown in green represent the selection window to define an accepted stub; a low-p_T rejected track is shown in red.
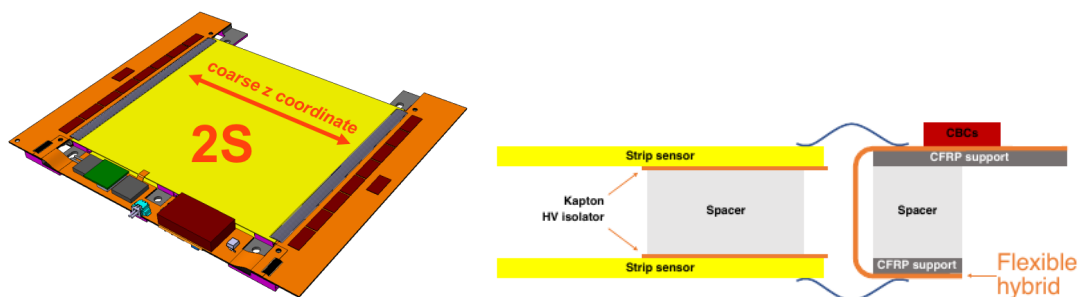
Figure 3: Left: sketch of the full-size 2S module. Right: cross section of the 2S module. The connection of the front end chips to strips of both the top and the bottom sensor via routing lines in the flexible hybrid (flex kapton circuit), which is bent around a stiffener/spacer sandwich [3], is visible.

The readout chips will provide the p_T discrimination logic described above. The window for hit matching can be set within the readout chip according to the p_T threshold to be used. For the 2S module, the readout chip is called the CMS Binary Chip (CBC) [5–9]. Each CBC has 254 readout channels with alternate channels connected to the top and bottom sensors in a module, as shown in Fig. 3 (right), so that coincidences between channels of the two sensors can be obtained.

The 2S module, shown in Fig. 3, consists of two sensors (n-type strips in p-type silicon substrate), support structures made from Al-CF (carbon fibre reinforced aluminium), two front-end hybrids [10], each with eight CBCs and one concentrator integrated circuit (CIC) that aggregates data from the CBCs, and a service hybrid for powering and output data serialization followed by opto-electrical conversion.

All prototype modules discussed in this paper use the second prototype of the CMS Binary Chip, the CBC2 [7–9]. The block diagram of the analogue front-end (FE) of the CBC2 ASIC is shown in Fig. 4. Three I²C registers are used to control the main settings of the analogue FE : V_{plus}, which controls the global DC baseline of the post-amplifier output, V_{offset} (labelled "Offset" in Fig. 4) for fine control of the baseline of the post-amplifier output for individual channels on the CBC2, and V_{CTH}, which controls the comparator threshold. The readout for the CBC2 chip is binary, thus it does not measure the amount of charge induced on each strip. If the charge on a strip exceeds the comparator threshold, a hit is registered.
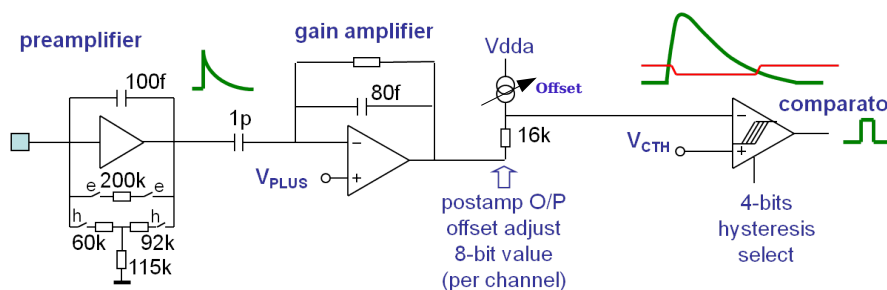

Figure 4: Block diagram of the analogue front-end (FE) of the CBC2 ASIC [7–9]. Three registers are used to control the analogue FE.

Table 2: Details of modules used in various beam tests.

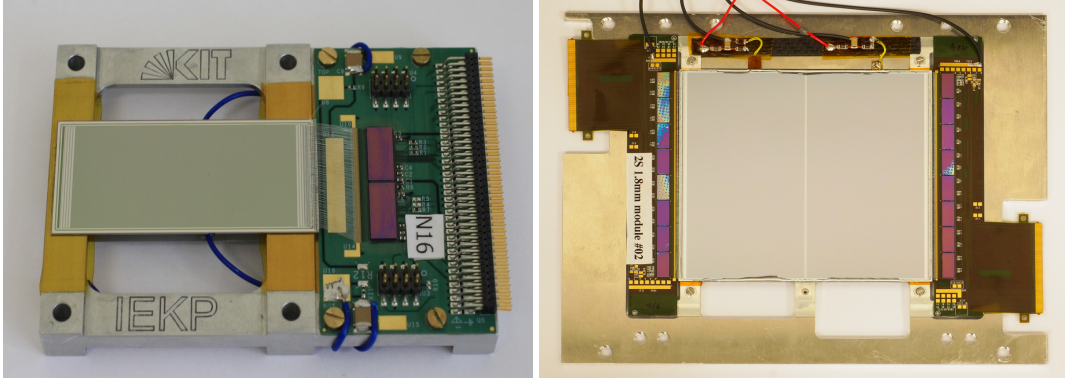| Module type	No. of CBC2s	Sensor active thickness	Sensor separation	Bias voltage	Beam Test facility
Non-irradiated mini-module	2	270 μm	2.75 mm	250 V	CERN, DESY, Fermilab
Irradiated mini-module	2	240 μm	3.05 mm	600 V	CERN
Full-size module	16	240 μm	1.80 mm	240 V	CERN, Fermilab

Figure 5: Left: the irradiated 2S mini-module assembled from a small prototype hybrid comprising two CBC2 readout chips and two silicon sensors with 254 strips of 5 cm length. Right: the full-size 2S module comprising two hybrids with eight CBC2 readout chips each and two full-size 2S sensors.

2.2 Prototype Detectors

Prototypes of the 2S module have been investigated at different test beam facilities (Table 2). For the beam tests described in Section 3, two small prototype modules and one full-size module have been studied. The strip sensors of the modules have 5 cm long n-type strips at 90 μm pitch on about 300 μm thick silicon sensors with p-type bulk. A negative voltage is applied to bias the sensors at the sensor backplane but in the following the absolute values of the bias voltage applied are quoted.

The small prototype modules, called mini-modules, consist of a version of the front-end hybrid housing two CBC2s. The hybrid is made of a rigid material with bond-pads on both sides and the sensors are wire-bonded to the top and bottom sides of it. This contrasts with the flex-kapton design used for full-sized modules that folds over the CF spacer to provide bond-pads for the bottom sensor [3, 11]. The sensors have been glued on a small frame made of aluminium. One mini-module was left unirradiated. The sensors of this module have an active thickness of 270 μm and their separation is 2.75 mm. The second mini-module, shown in Fig. 5 (left), with an active sensor thickness of 240 μm and a sensor separation of 3.05 mm, was irradiated with 23 MeV protons at Irradiation Center Karlsruhe [12] to a fluence of 6×10^{14} n_{eq}/cm^2 with an annealing of approximately two weeks at room temperature. The maximum expected fluence for the innermost layer of the 2S modules of the OT is 3×10^{14} n_{eq}/cm^2 [3]. This value corresponds to 3000 fb^{-1} of proton-proton (pp) collisions at $\sqrt{s} = 14$ TeV assuming a total inelastic cross section, σ_{pp}, of 80 mb.

The current-voltage characteristic of the sensors before and after irradiation can be seen in Fig. 6. The effect of irradiation is reflected by an increase of the leakage current by three orders of magnitude.

The full-size module consists of two sensors of about 10 cm $\times$ 10 cm, with two columns of 1016 strips each. The active thickness of each sensor is 240 μm and the sensors are separated by
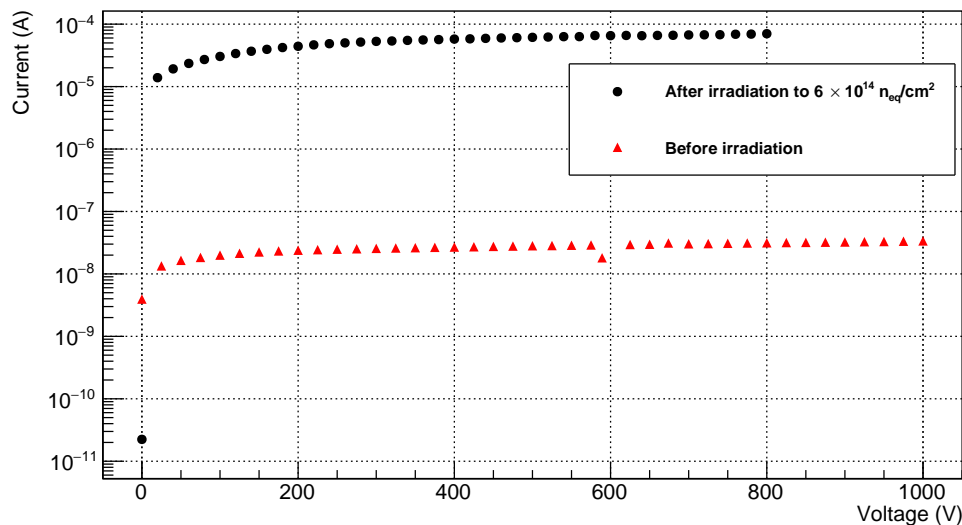
Figure 6: The current-voltage characteristic of a sensor of the mini-module before (red) and after (black) irradiation to 6×10^{14} n_{eq}/cm^2, showing the increased current after irradiation. The measurements were taken at $-20°\,C$ and $20°\,C$ for the irradiated and non-irradiated sensors, respectively.

1.8 mm. Each of the front-end hybrids on both ends of the module houses eight CBC2s. A flex hybrid is used to provide bond-pads for the top and bottom sensors (Fig. 3). The module is built with a rotation angle between the strips of both sensors of below 400 μrad. This module is shown in Fig. 5 (right).

3 Beam Test Infrastructure

The prototype modules have been studied at beam test facilities at CERN, Fermilab and DESY. In all of the facilities, the detector under test (DUT) is placed within a tracking detector, referred to as 'telescope' in the following. The telescope provides a reference to reconstruct the tracks of the incident particles. The beam test facility at CERN is described in detail in the following section, and the key features of the DESY and Fermilab test beam facilities are highlighted. The data acquisition systems (DAQ) of the three facilities are also described.

3.1 Beam Test Setup

A schematic diagram of the setup at CERN is shown in Fig. 7. Data were collected using a 120 GeV pion beam. The EUDET telescope [13] used in the CERN beam test of the 2S prototype modules is a tabletop tracking detector composed of six planes of MIMOSA-26 [14] silicon pixel sensors for accurate track reconstruction, a fast-timing reference plane (FE–I4) [15] for accurate timing resolution, and a pair of crossed scintillators with photomultiplier tubes (PMTs) located at either end of the telescope for trigger generation. The six MIMOSA-26 sensor planes, each covering an active area of 10.6×21.1 mm^2, consist of 50 μm thick 18.4 μm $\times$ 18.4 μm square pixels arranged in 576 rows and 1152 columns. The fast-timing plane covers an active area of 16.8×20.0 mm^2 and consists of 200 μm thick pixels arranged in 336 rows and 80 columns read out by the FE–I4 chip, which was designed for the innermost layer of the upgraded pixel detector of the ATLAS experiment. Each sensor plane is mounted inside a 20 mm thick aluminium

jig, and two sets of three jigs are attached via rail systems to the upstream/downstream arms of the telescope. The minimum distance between sensor planes is defined by the thickness of the aluminium jig (and is therefore 20 mm), and the maximum distance between sensor planes is defined by the length of each arm (150 mm for equidistant spacing between the sensor planes). The jigs are cooled to a constant temperature of $16°C$ to increase the stability of operation.
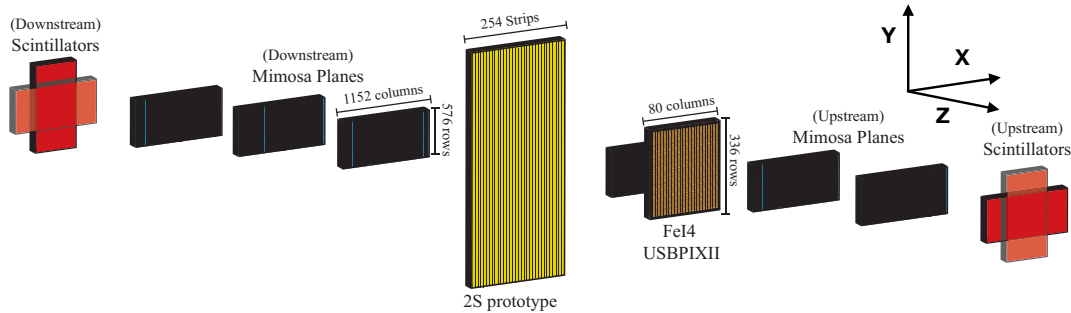

Figure 7: Schematic drawing of the beam test setup at CERN showing the three detector systems used to characterize the performance of the 2S prototype module: the 6 MIMOSA planes, the ATLAS FE–I4 plane and the four scintillators used to generate the NIM trigger. The DUT is placed within the telescope system as shown.

The synchronization of the data streams from the three detector systems (the 2S prototype, the MIMOSA-26 sensor planes, and the FE–I4 plane) is performed by an FPGA-based Trigger Logic Unit (TLU) [16, 17]. During the beam tests, dedicated NIM logic is used to generate a trigger signal using the output signals from the two pairs of crossed scintillators at either extremity of the EUDET telescope. This trigger signal is provided as input to the TLU, which distributes this signal to the DUT and to the telescope's sensor planes. A simple handshake protocol is used by the DAQ system to maintain synchronization among the different detector systems. The detector systems assert busy signals on separate lines, which inhibit triggers from the TLU until all of the lines are cleared. No new triggers are sent by the TLU until all detectors drop their busy-lines. This ensures that detectors with different dead-times can be triggered and read out synchronously. In addition, the TLU can send a timestamp for each trigger via a dedicated clock-data line, or it can receive a back-pressure (veto) signal from the DUTs on the same line. The additional ATLAS FE–I4 plane is used to improve the timing resolution of the telescope by associating the FE-I4 hits with the individual hits in the 115.2 μs rolling-shutter frame of the telescope during event building. This allows the multiple tracks in a telescope frame to be correlated to individual triggers. Because the FE-I4 readout has no dead-time and runs on an internal 40 MHz clock, the required time resolution of 25 ns for the CBC DAQ is achieved. The data streams from the telescope and the FE-I4 are sent to the EUDAQ [13] online software via the TCP/IP protocol [18]. The two streams are stored together in the same format in a file, which makes the reconstruction easier in the EUDET [19] framework.

The beam test at DESY uses the EUDET based telescope called DURANTA [13], similar to the one used during the CERN beam test. It also uses six MIMOSA-26 pixel sensors with four crossed scintillators for triggering and a TLU, however it was equipped with a CMS Phase-1 pixel [20] module as a timing reference plane instead of the FE–I4. The data were collected with a positron beam of 5 GeV energy.

The Fermilab Test Beam Facility, or FTBF [21], is equipped with two silicon telescopes aligned along the beam line and configured to operate synchronously. It has a pixel telescope assembled from eight planes and a telescope with strip modules made up of 14 detector planes. The strip telescope increases the coverage of the pixel telescope and improves its tracking perfor-

mance. The trigger is generated by a coincidence signal of three scintillation counters, one placed in front and two placed behind the telescopes. The synchronization of the data streams from the two telescopes and the 2S module is performed by a Fermilab-designed FPGA-based trigger board. The data are taken with a 120 GeV proton beam.

3.2   Data Acquisition System

The DAQ system for the CBC2 modules at CERN and Fermilab test beams is based on the CERN Gigabit Link Interface Board (GLIB) [22] μTCA Advanced Mezzanine Card (AMC). Different firmware versions are used to read data from the 2 and 16 CBC2s on the tested modules. Control signals and readout data are exchanged between the GLIB and the control PC via the IPBus [23] protocol, whereas trigger, busy and veto signals are interfaced to the TLU/Fermilab equivalent via a dedicated five-channel I/O FPGA Mezzanine Card (FMC). A simple block diagram of the different components of the DAQ system is shown in Fig. 8.
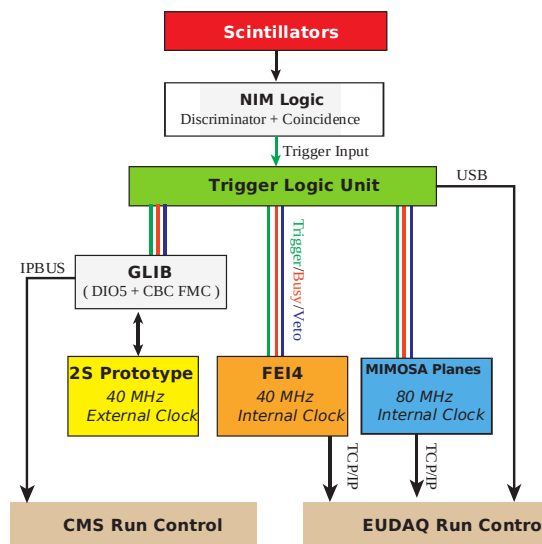

Figure 8: Block diagram of the DAQ system used in the **CERN and Fermilab** beam test setups. The correlation of the data from the two DAQ chains is described later in Section 5.

An external high-precision clock generator was used to provide the clock signals to the GLIB via the same FMC that connects to the TLU. The CBC2 data are processed and formatted by the firmware and then sent to a XDAQ [24] application that formats events in a CMS compatible format and stores the data for later processing within the standard CMS reconstruction software, CMSSW [25]. The binary raw data stream is also stored and can be used for online data quality monitoring.

The beam test at DESY used a novel DAQ system, based on the FC7 [26] card. The FC7 hosts a Kintex-7 FPGA and comes with a system firmware allowing for communication with other devices on the FC7 card and IPBus communication. A DIO5 FMC is used to send trigger and busy signals via LEMO connectors. These are fed into a custom-built LVDS converter box and sent to the TLU via a standard RJ45 connector.

4 Preparations for Data-taking

4.1 Pedestal and Noise

The pedestal and noise values of an individual channel in a system with binary readout can be inferred from a channel's S-curve. An S-curve is obtained by measuring the noise occupancy as a function of the comparator threshold (V_{CTH} in Fig. 4). The comparator threshold has been measured in V_{CTH} DAC units. One V_{CTH} DAC unit corresponds to 375 electrons, as measured using an X-ray source. The noise occupancy is given by the fraction of triggers for which a given channel registers a hit. Higher numerical values of V_{CTH} correspond to lower thresholds in the CBC2. Figure 4 also shows the per-channel 8-bit DAC used to control the offset of the output voltage of the second amplification stage to compensate for any channel-to-channel variations.

The pedestal value and the channel noise are extracted directly from the S-curve either by fitting the curve with a sigmoid of the form

$$f(x, \mu, \sigma) = \frac{1}{2}\left[1 + \text{erf}\left(\frac{x - \mu}{\sqrt{2}\sigma}\right)\right], \tag{1}$$

or by numerically differentiating it. The mean parameter, μ, in Eq. 1 (or the mean of a Gaussian fitted to the differential histogram) then corresponds to the pedestal and σ (or the RMS of a Gaussian fitted to the differential histogram) corresponds to the noise. An example of an S-curve recorded for a CBC2 and the corresponding differential histogram are shown in Fig. 9. Both methods return similar (i.e. consistent within 3σ) values for the pedestal and noise. The pedestal value, obtained from fitting the left plot of Fig. 9 with a sigmoid function, is 120.0 ± 0.1 V_{CTH} DAC units. A pedestal value of 119.3 ± 0.2 V_{CTH} DAC units has been obtained by fitting the distribution shown in Fig. 9, right, with a Gaussian function. For the noise, 2.12 ± 0.06 V_{CTH} DAC units and 2.14 ± 0.15 V_{CTH} DAC units are obtained, respectively.
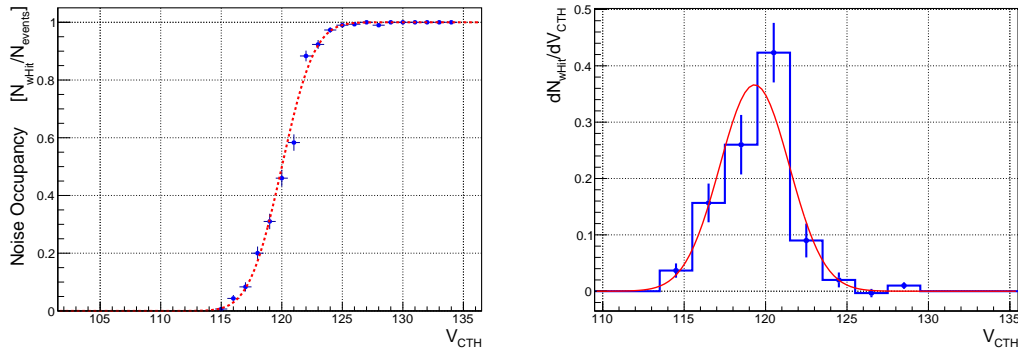

Figure 9: S-curve measured for a single input channel on one of the two CBC2s on a non-irradiated prototype module at room temperature with the sensor biased at 250 V. On the left the measured data are shown along with a fit to the measured data performed using Eq. 1, while on the right the differential histogram is shown with the corresponding Gaussian fit.

Figure 10 shows the uniformity of the front-end response after adjustment of the individual channels' offsets. The pedestal and noise values were extracted from the fits to the individual channels' S-curves using Eq. 1. The channel-to-channel variation in the pedestal, defined as the RMS of the measured distribution, is measured to be 0.30 ± 0.01 and 0.37 ± 0.02 V_{CTH} DAC units for the first and second CBC2, respectively. The mean noise was found to be 1.36 ± 0.06 and 2.38 ± 0.60 V_{CTH} DAC units for the first and second CBC2, respectively. The same figure also clearly shows that 11 of the strips connected to the second CBC2 on the hybrid are

significantly noisier than the rest. These 11 strips are included in the noise figure quoted for the second CBC2. The strips exhibiting a value of noise larger than 3 V_{CTH} DAC units (1125 electrons) are not considered for analysis.
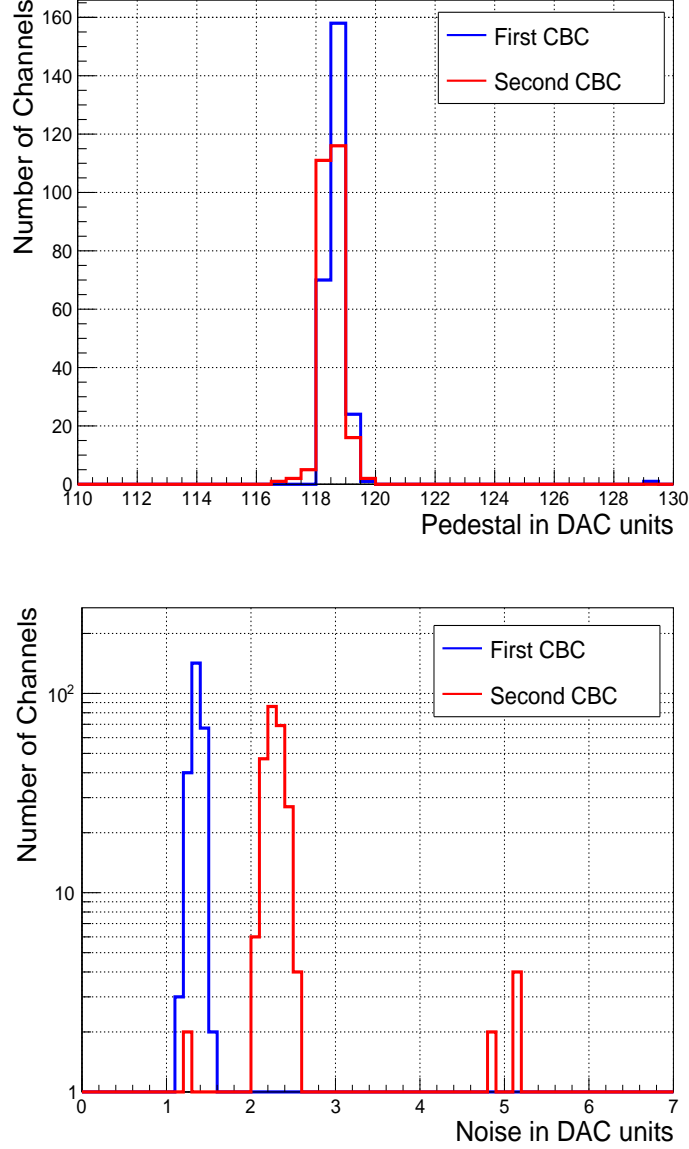

Figure 10: Pedestal (top) and noise (bottom) for both CBC2s on a prototype module.

4.2 Latency Scans

After the pedestal and noise scans, two latency scans, one for data and one for stubs, were carried out. The data latency, measured in units of 40 MHz clock cycles and set using an on-chip configuration register, defines the position in the on-chip RAM from which the data are read upon reception of a trigger. The stub latency, also measured in units of 40 MHz clock cycles and set by a configuration register in the back-end FPGA, defines the delay between hit and stub data arriving at the back-end of the data acquisition system and is required to assemble the data at the back-end.

The resolution of the data latency measurement was improved using a high-resolution time-

to-digital converter (TDC) in the back-end FPGA. The TDC measures the time of arrival of the trigger signal at the back-end with respect to the 40 MHz clock edge in time slices of 3.125 ns, using a 3 bit counter operating at 320 MHz. The results of the latency scans performed in the CERN beam test are shown in Fig. 11. These scans were used to identify the stub and data latencies to use during data taking by counting the number of stubs and hits contained in the data stream for a fixed number of triggers and selecting values for the data and stub latency that maximize the fraction of events containing stubs and hits, respectively. Both scans were performed at a threshold of 113 DAC units (3σ away from the pedestal). For further data taking, the data latency and stub latency were fixed at 13 and 4, respectively, as shown by the dashed lines in Fig. 11.
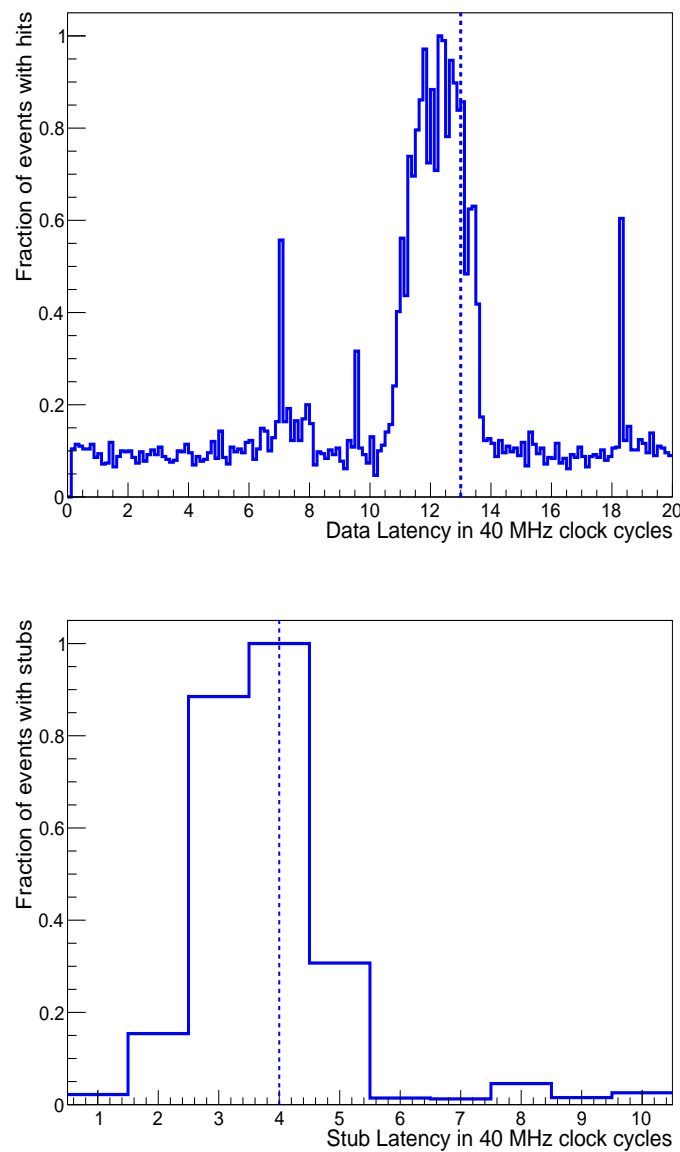

Figure 11: Results from data (top) and stub (bottom) latency scans. The TDC phase gives fine resolution within a 40 MHz clock cycle (1/8). The dashed lines indicate the chosen values.

5 Reconstruction

Dedicated software is used to reconstruct the data collected from the telescope system and the DUT. Initially, the reconstruction of tracks of the incident particle is carried out using the hits in the telescope system. The reconstruction of data from the DUT involves the formation of clusters and stubs using the hits from the individual channels. The reconstructed tracks are then extrapolated to the DUT, and the estimated position of the track on the DUT is computed. Using this information, an alignment is performed to correct for the relative offset in position of the DUT with respect to the telescope system. The reconstruction of tracks from the telescope data, clusters and stubs from the DUT data, and alignment procedures are described in the following sections.

5.1 DUT Reconstruction

The schematic diagram for the processing of the DUT data is shown in Fig. 12. The raw data received from the 2S modules by the FPGA are converted to the CBC2 event format by the DAQ software and served to the online Data Quality Monitoring (DQM) system. The raw data are also sent to the CMS event builder (EVB) [27] which provides data in the Event Data Model (EDM) format [28, 29]. The EDM data are then processed by the CMS offline software, CMSSW [25], to produce clusters and stubs used in the offline analysis. Hits in adjacent strips of the DUT are combined to form a cluster. The number of strips included in a cluster is called the cluster width. The cluster position is defined by the center of the cluster rounded down to an integer strip number. The CBC2 reconstructs stubs, by calculating the cluster positions in integer strip numbers. However, it outputs only the information that a stub was present, not its position (in contrast to later versions of the chip, which include this functionality). Therefore the stub reconstruction is done offline, by emulating the logic in the CBC2. Clusters with cluster width greater than 3 are excluded from stub formation. The difference in position (in number of strips) of the clusters in the bottom sensor is calculated with respect to clusters in the top sensor. If this difference is less than the predefined window, an offline stub is formed. The position of the stub is defined as the position of the cluster in the bottom sensor seeding the stub. As the DAQ systems for the telescope and for the DUT are different, an additional processing step is needed to synchronize the events coming from telescope and DUT data streams by matching the individual trigger numbers using the ROOT data analysis framework [30].

5.2 Tracking

Tracks from the EUDET telescope are reconstructed in the EUTelescope [13] framework using MIMOSA-26 planes. A database of noisy pixels (pixels with exceptionally high occupancy) is built and used to exclude such pixels from subsequent steps of the analysis. Clusters are built according to the nearest neighbour search algorithm, which iteratively joins adjacent pixels with hits to form a cluster. A *"pre-alignment"* is performed in the telescope global frame, correcting only for the misalignment in X and Y directions (as shown in Fig. 7). The output of this step is used to constrain the alignment step itself, based on solving exact matrix equations with the Millipede II framework [31]. Shifts in X, Y and Z coordinates and 3 Euler rotation angles for each Mimosa plane are corrected for. Tracks are then reconstructed with a Deterministic Annealing Filter (DAF) algorithm [32, 33], where all hits within a given radius are used for the track reconstruction.

Tracks reconstructed with the DAF are further cleaned to remove any duplicates, defined as two or more tracks with X and Y coordinates at the FE–I4 plane less than 1 μm apart.

While Mimosa planes are read out with a rolling shutter having a window of 115 μs, the max-
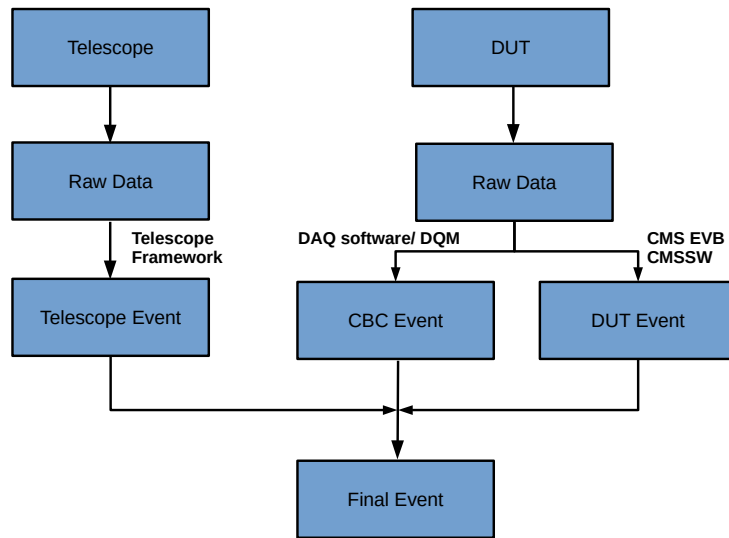
Figure 12: A schematic representation of the data processing for the beam tests at CERN. The Telescope event contains information about the incident track parameters. The DUT event contains the information of the hits as read from the DUT and also the clusters and stubs reconstructed using offline software. The CBC event contains the information about CBC errors. Data from all three sources are merged and stored into a single file for offline analysis.

imum acquisition rate for the DUT and the FE–I4 plane is 40 MHz. The presence of a hit in the FE–I4 plane that can be matched to the track is used as a timestamp, which largely reduces track combinatorics. Residuals at the FE–I4 plane are used to determine a nominal distance between the track impact point and the FE–I4 hit. The residuals are fitted with a step rectangular function convolved with a Gaussian smearing. The maximum distance to accept a track is set to half the width of the step function, compatible with the FE–I4 pitch, plus two times the width of the Gaussian, compatible with the track pointing resolution.

Track reconstruction and telescope alignment at the Fermilab test beam facility are performed using a single dedicated software package [21] that provides a graphical interface to execute the various steps. An iterative algorithm implements a least-squares minimization to compute 1st-order roto-translational corrections using tracks reconstructed with a preliminary description of the geometry.

The reconstruction of beam test data at DESY follows a similar procedure to that used for beam tests at CERN. The main difference is that the entire reconstruction is performed within the EUTelescope framework and that the General Broken Lines (GBL) [34] algorithm for alignment is used. The GBL algorithm is required to account for the increased multiple scattering of the comparatively low-energy particles available at the DESY beam test facility.

5.3 DUT Alignment

The DUT alignment procedure consists of minimizing the residuals at the DUT plane to constrain the degrees of freedom of the system:

$$\chi^2 = \frac{1}{N} \sum_{i=0}^{N} \left(\frac{x_{\text{DUT}} - x_{\text{TkAtDUT}}}{\sigma_{tkres}} \right)^2,$$

where x_{DUT} is the hit position in X and x_{TkAtDUT} the position of the hit as derived from the track extrapolation to the DUT location, while σ_{tkres} is the telescope pointing resolution. The sum runs over all events in which at least one cluster in the DUT and one track are reconstructed. For each event the closest pair is selected. To remove outliers, the sum is further restricted to events where the residual $|x_{\text{DUT}} - x_{\text{TkAtDUT}}|$ is less than $3\sigma_{tkres}$ away from the mean value of a Gaussian fit of the residual distribution.

The track impact point on the FE–I4 plane is propagated to the first sensor plane of the DUT, which corresponds to the plane of the sensor facing the beam direction, including degrees of freedom for the X position of the first plane, Z position of the first plane, θ angle around the Y-axis, and the distance between the two sensor planes of the DUT. This procedure eliminates the sign degeneracy of the θ angle. For efficiency studies reported in Section 6, a track is matched to a hit, cluster or stub on the DUT if the residual, $|x_{\text{DUT}} - x_{\text{TkAtDUT}}|$, is less than $3\sigma_{tkres}$.

6 Results

After calibration, the threshold (V_{CTH}) and the angle of rotation of the DUT with respect to the beam were varied in suitable step sizes and the properties of hits, clusters and stubs were studied. The axis of rotation of the DUT was the Y axis, as shown in Fig. 7.

A scan of V_{CTH} was performed at vertical beam incident and measurements of the cluster and stub efficiencies were carried out as a function of a number of functional parameters to fully characterize the mini-modules (Sec. 6.1) and the full-size module (Sec. 6.2).

6.1 Performance of Mini-modules

Figures 13 and 14 show the average number of hits and clusters on the non-irradiated and irradiated mini-modules, respectively. Lower numerical values of V_{CTH} mean a higher signal threshold, as mentioned in Section 4.1. For the non-irradiated mini-module, the average number of hits/clusters increases as V_{CTH} is increased and a plateau with a value close to 1 is visible, up to V_{CTH} values of about 110. However, for the irradiated module, the average number of hits/clusters is mostly less than 1 as V_{CTH} is increased. This indicates that, for a given value of V_{CTH}, we see a lower number of hits/clusters in the irradiated mini-module as compared to the non-irradiated one. As the V_{CTH} setting is increased further ($\gtrsim 110$), the noise increases in both mini-modules, leading to a sharp rise in the average number of hits/clusters. Differential histograms of cluster occupancy as a function of V_{CTH}, derived by numerically differentiating the distributions of the cluster occupancy as shown in Fig. 14, are shown in Fig. 15. The differential distributions show an inverted Landau distribution, caused by the actual signal generated from the incident particle, and a noise peak. Comparing the differential distributions, it can again be seen that the total number of clusters is lower in the irradiated mini-module. The loss in the number of clusters for the irradiated mini-module as seen in Fig. 14 and Fig. 15 indicates that the charge collection in the irradiated mini-module is worsened due to radiation induced effects. Along with radiation induced effects, the lower sensor active thickness of 240 μm for
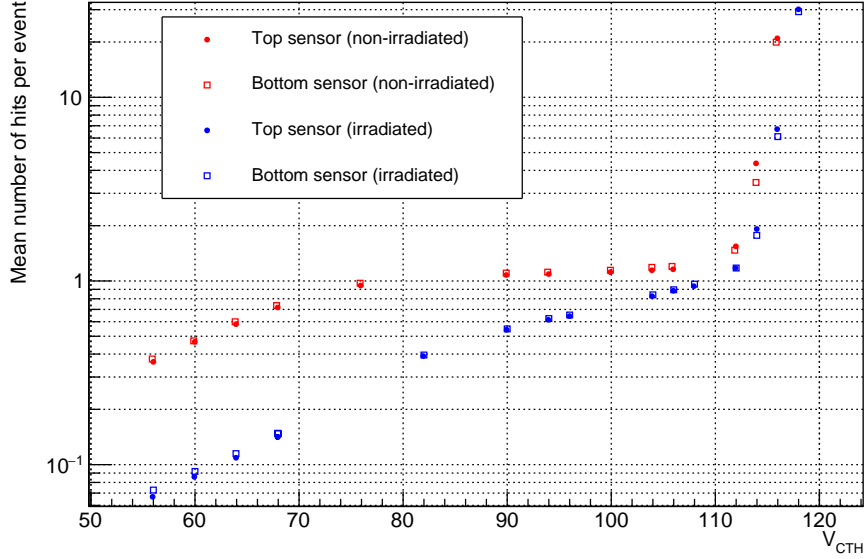
Figure 13: Average number of hits per event on non-irradiated and irradiated sensors as a function of V_{CTH}. A bias voltage of 250 V (600 V) was applied to the non-irradiated (irradiated) mini-module.

the irradiated module, compared to 270 μm of the non-irradiated module, also leads to lower charge collection. By choosing appropriate V_{CTH} values of 106 and 110 DAC units for the non-irradiated and irradiated module, respectively, signals from incident particles can be collected preferentially.

The cluster efficiency, defined as the ratio between the number of events with a cluster matched to a track in a single track event and the total number of events with a single track, is then measured as a function of V_{CTH} for different values of the trigger phase (TDC), to check for a potential dependency. The cluster efficiencies for one of the sensors of the non-irradiated and irradiated mini-modules are shown in Fig. 16. The lower charge collection in the irradiated module results in a smaller effciency plateau (Fig. 16, bottom) compared to the non-irradiated module (Fig. 16, top). As the V_{CTH} increases further (> 110), the efficiency starts to degrade for both the mini-modules due to increase of noise. However, the higher noise level in the irradiated module increases the probability of the track getting matched to a noisy cluster and results in a higher efficiency for the irradiated module in the high V_{CTH} region. A small dependency on the trigger phase is present for both sensors and is more evident at lower V_{CTH}. A trigger phase is present in the CERN beam test because the trigger signal is asynchronous with respect to the 40 MHz clock that drives the readout electronics.

Because there is no magnetic field, the dependence of the mini-module performance on the transverse momentum of tracks is emulated by rotating the DUT with respect to the beam direction. As the incident angle (referred to as α) of the particles increases, the charge deposited is shared by multiple strips and hence the cluster width is expected to increase, which is shown in Fig. 17. This effect is less evident on the irradiated module due to the radiation induced defects both in the sensor bulk and on the surface, that change the electric field inside the sensor. This leads to a modification of the charge sharing and further to a higher average cluster size at normal incidence. The same effect is also evident from the distribution of the fraction of clusters with different strip multiplicities, as shown in Fig. 18. The non-irradiated
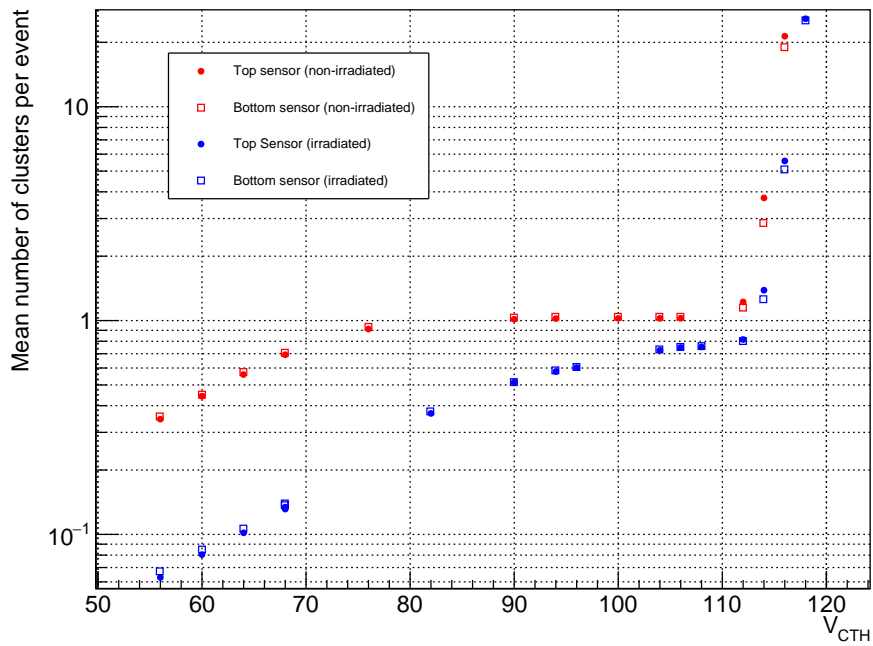
Figure 14: Average number of clusters per event for non-irradiated and irradiated sensors as a function of V_{CTH}. A bias voltage of 250 V (600 V) was applied to the non-irradiated (irradiated) mini-module.
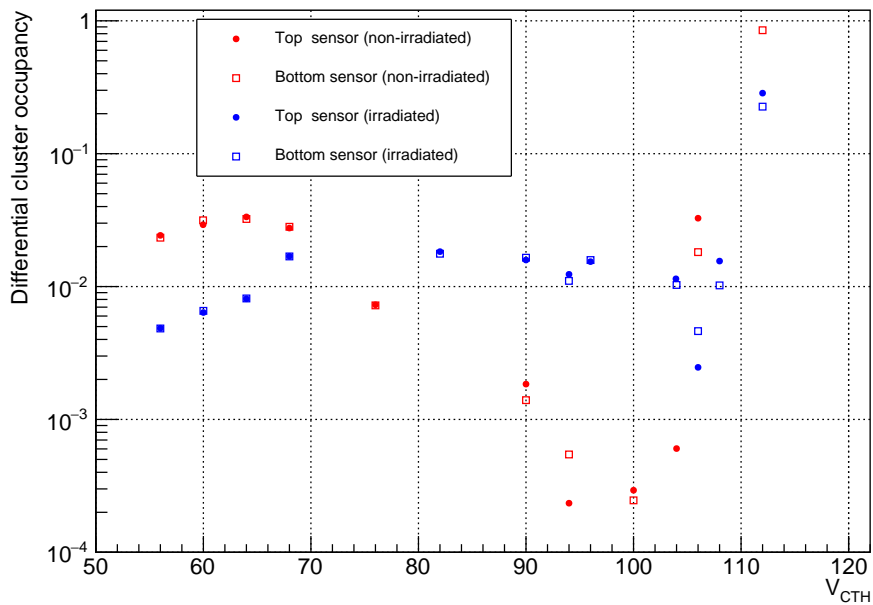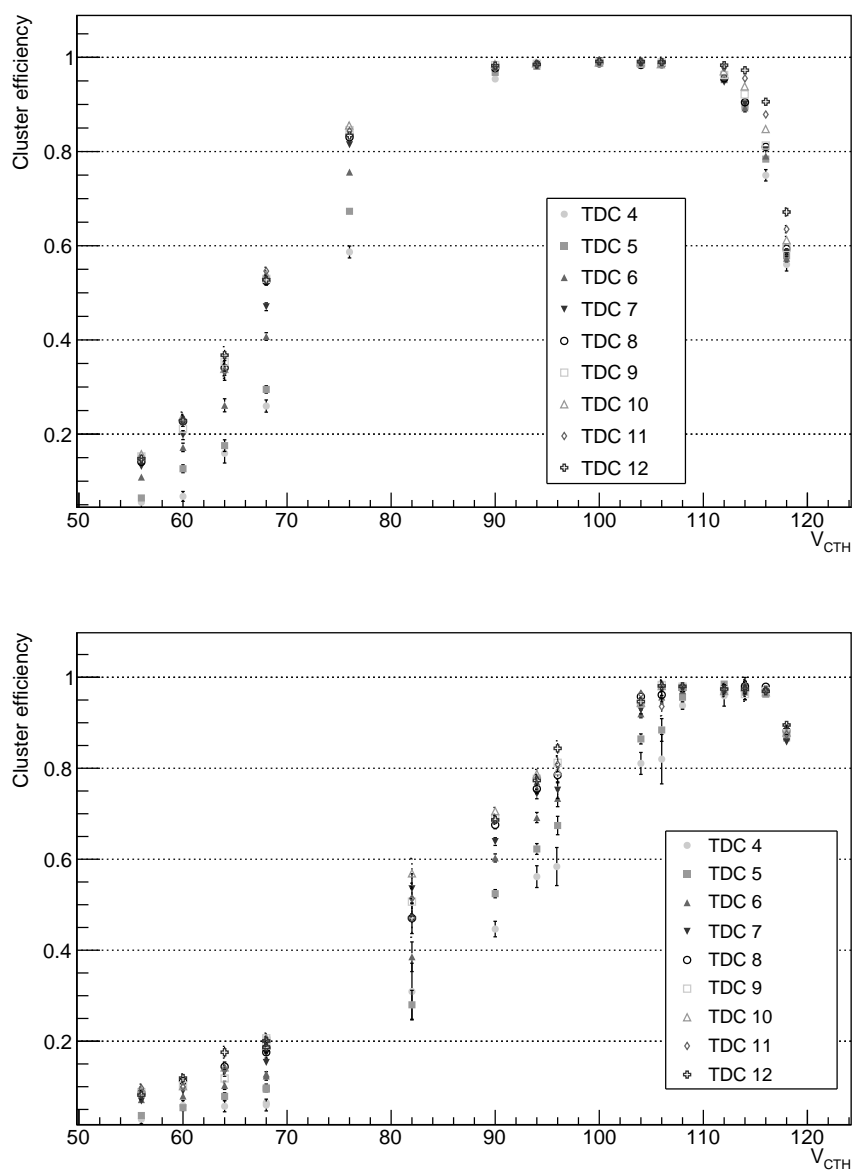

Figure 15: Differential cluster occupancy for non-irradiated and irradiated sensors as a function of V_{CTH}. A bias voltage of 250 V (600 V) was applied to the non-irradiated (irradiated) mini-module.

Figure 16: Cluster efficiency of the non-irradiated (top) and irradiated (bottom) 2S mini-modules presented as a function of V_{CTH} for different phase differences between trigger and readout clocks. A bias voltage of 250 V (600 V) was applied to the non-irradiated (irradiated) mini-module.
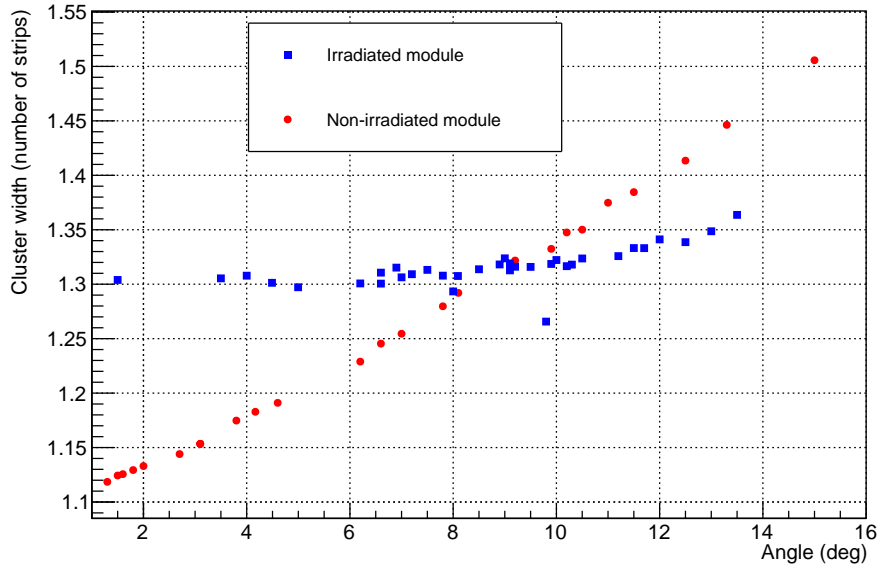
Figure 17: Mean cluster width of non-irradiated and irradiated 2S mini-modules as a function of the beam incident angle. Due to radiation induced defects, charge sharing is higher in the irradiated module, leading to a larger mean cluster size. A bias voltage of 250 V (600 V) was applied to the non-irradiated (irradiated) mini-module.

module shows a correlation between the cluster fractions and the angle. This dependence is much less significant for the irradiated module.

In Fig. 19 the cluster efficiencies for different TDC values as a function of the DUT rotation angle for the two modules are shown. The dependency on the trigger phase is negligible and the mean cluster efficiency for the full range of the angular scan is $99.56 \pm 0.01\%$ and $98.21 \pm 0.02\%$ for the non-irradiated and irradiated modules, respectively.

For the CMS field strength of $B = 3.8\,\text{T}$, the relationship between the beam incident angle (α) and the emulated transverse momentum p_T of the traversing particle for a radial position of the module (R) is given by $p_T\,[\text{GeV}] \approx \frac{0.57 \cdot R[\text{m}]}{\sin(\alpha)}$. The stub efficiency, defined as the ratio of the number of events with stubs matched to a track in single track events to the number of events with a single track, was measured for each incident angle. Tracks and stubs must match within 4σ of the spatial resolution. The stub efficiency of the two mini-modules as a function of effective p_T (beam-incident angle) is shown in Fig. 20. For larger angles of incidence the relative shift in cluster position in the two sensors of a module is larger, which leads to lower probability of correlating them as stubs. The stub efficiency drops for larger angles for this reason. A stub correlation window of 5 strips is used. A radius of 60 cm was used for the calculation of the effective p_T from the beam incident angle. The turn-on curve is different for the two modules due to different sensor spacing.

The turn-on curve was fitted with an error function of the form

$$f(p_T) = 0.5A\left(1 + erf\left(\frac{p_T - p_{T\mu}}{\sigma_{p_T}}\right)\right),$$

where A is the efficiency at the plateau, $p_{T\mu}$ is the turn-on threshold for which the efficiency is 50%, and σ_{p_T} is the width of the Gaussian in the error function. The p_T resolution is defined as
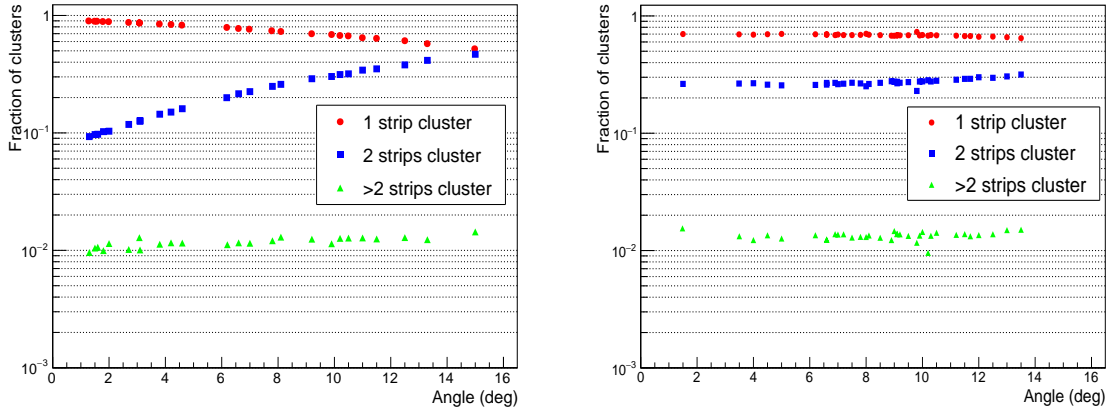
Figure 18: Fraction of clusters with different strip multiplicity; (left) non-irradiated module; (right) irradiated module. A bias voltage of 250 V (600 V) was applied to the non-irradiated (irradiated) mini-module.

the ratio of the width of the Gaussian to the p_T value at 50% of the plateau height, or $\sigma_{p_T}/p_{T\mu}$. For the non-irradiated module, the turn-on threshold is 1.88 GeV with a p_T resolution of 5%, whereas the expected turn-on threshold is 2 GeV. The plateau efficiency for the non-irradiated module is 99%. The high plateau efficiency with sharp turn-on demonstrates that the module can reject tracks with $p_T < 2$ GeV efficiently. For the irradiated mini-module, the plateau efficiency reaches 97% with a p_T resolution of 6%. This shows that the stub finding logic of the 2S modules will work even after being irradiated to a fluence of 6×10^{14} n_{eq}/cm^2, which is twice the expected fluence for the first layer of 2S modules. The stub efficiency measured using data collected at the DESY test beam facility with the non-irradiated mini module is found to be 99%.

For the irradiated module three angular scans were performed, each with different stub correlation windows. As shown in Fig. 21, the turn-on curve of the efficiency depends on the selected correlation window, while the efficiency plateau does not.

6.2 Performance of the Full-size Module

For the full-size 2S module, the primary goal was to check the uniformity of the response across all strips. Figure 22 (top) shows the stub efficiency per strip for the full-size 2S module. The module was operated at a bias voltage of 250 V and V_{CTH} was set to 115 DAC units. The analysis techniques used are the same as reported for the mini-modules. The region between strips 185 and 239 has no data because it was not scanned by the beam. The large statistical uncertainty in efficiency at the edges is due to the limited data collected for the scans performed at the module edges. The mean stub efficiency extracted from a linear fit, where the asymmetric errors on each measurement are taken into account, is 97.4%, and the strip-to-strip variation of the stub efficiency was found to be 1.3%. The efficiency is approximately 2% lower than that measured in the 2S mini-module. The difference is due to a different operational configuration of the modules and a possible remaining contamination of events for which the module was not synchronized with the telescope. The stub efficiency per chip is shown in Fig. 22 (bottom). The results demonstrate that the response of the full-size 2S module is uniform across strips. The stub efficiency as a function of effective p_T for the full-size 2S module measured with data collected at the Fermilab test beam facility is shown in Fig. 23. The correlation window used for stub formation was set to 5 strips. The figure shows that the behaviour of the full-size module
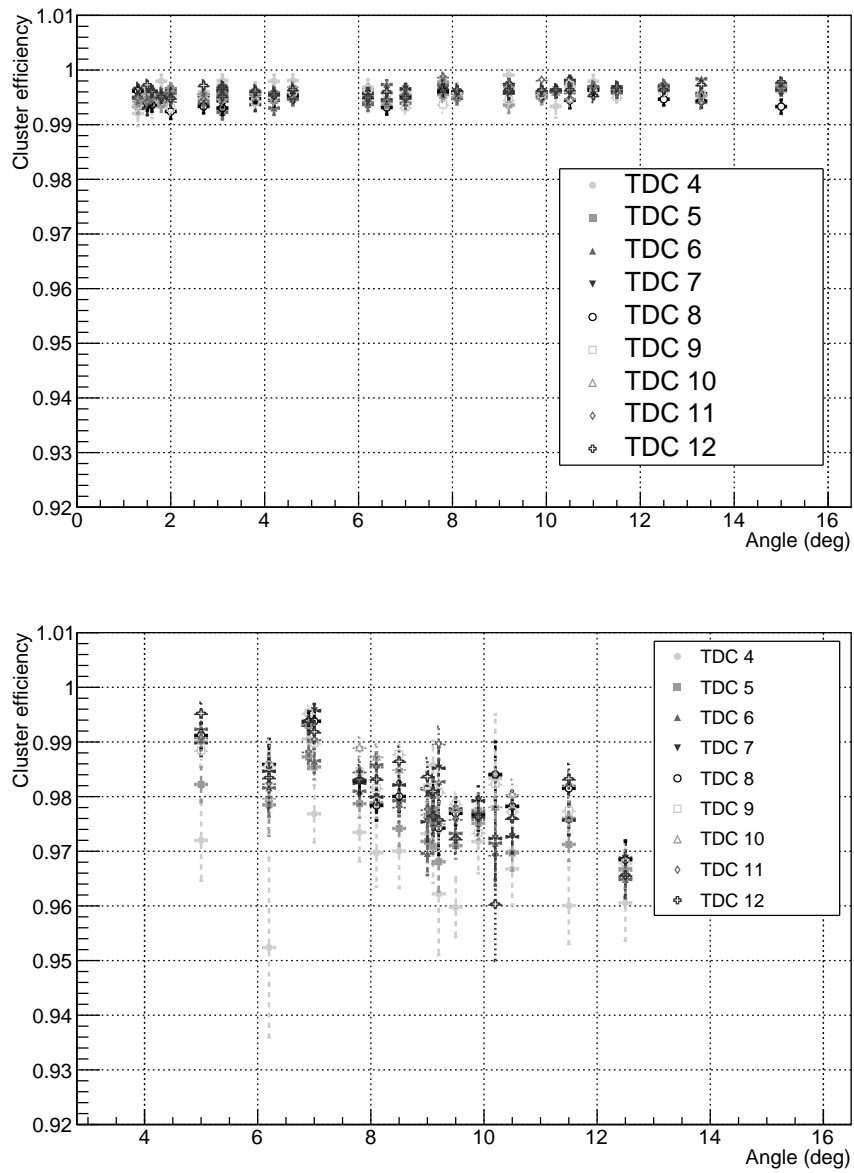
Figure 19: Cluster efficiency of the non-irradiated (top) and irradiated (bottom) 2S mini-modules as a function of the beam incident angle for different TDC phases. A bias voltage of 250 V (600 V) was applied to the non-irradiated (irradiated) mini-module.
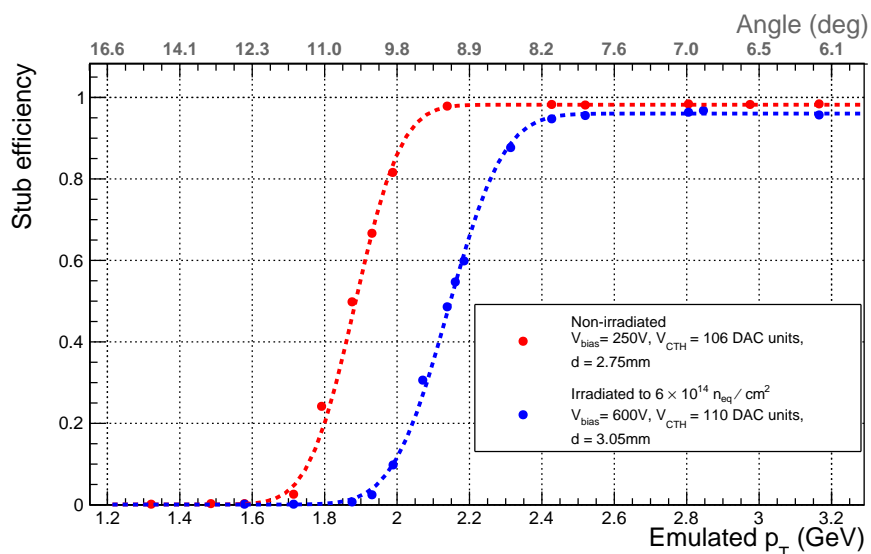
Figure 20: Stub efficiency for the irradiated (blue) and non-irradiated (red) modules as a function of the beam incident angle. As expected, for larger angles of incidence, which corresponds to smaller effective p_T, the stub efficiency drops. A radius of 60 cm was used for the calculation of p_T from the beam incident angle which is approximately the radius at which the first layer of 2S modules will be installed. The stub correlation window is set to 5 strips.
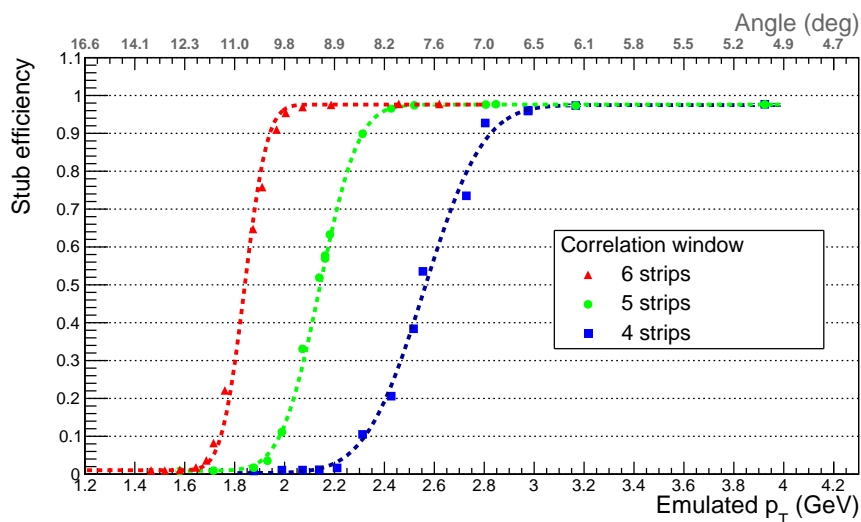

Figure 21: Stub efficiency comparison of different angular scans with different correlation windows for the irradiated module. The choice of window size leads to a shift in the turn-on p_T, but the efficiency at the plateau remains the same. A bias voltage of 600 V was applied to the irradiated mini-module.
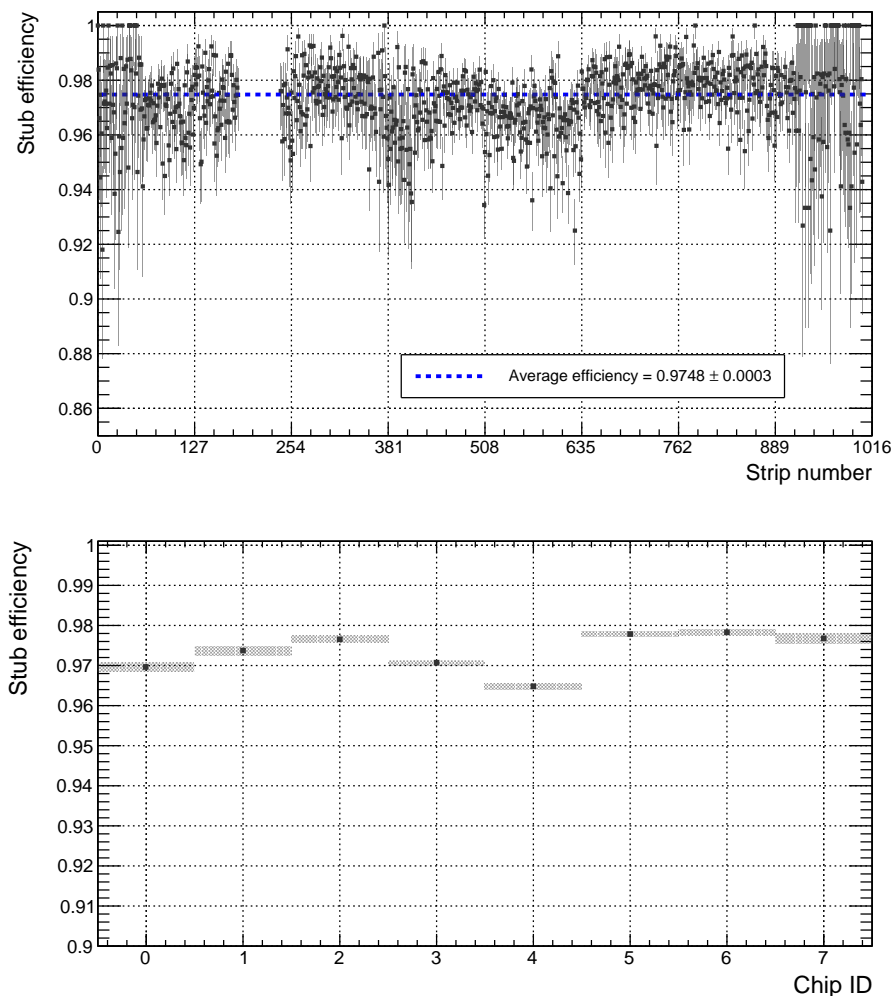
Figure 22: Stub efficiency of a full-size 2S module measured at the CERN beam test facility. The module was operated at a bias voltage of 250V and the V_{CTH} value was set to 115 DAC units. Top: stub efficiency per strip, bottom: stub efficiency per chip computed using data from strips scanned by the beam.

is similar to that of the mini-modules. From the fit, a turn-on threshold of 1.2 GeV is obtained with a p_{T} resolution of 7.9%. The turn-on threshold is lower compared to the non-irradiated mini-module since the sensor separation is smaller. The efficiency at the plateau is 99%.

7 Summary

A new silicon strip tracker will be installed in CMS for the HL-LHC period. The new Outer Tracker will comprise novel detector modules with two closely spaced sensors and a new front-end ASIC that is capable of correlating hits between the sensor layers. The performance of 2S prototype modules has been characterized at three test beam facilities. The presence of tracking detectors at these facilities has allowed for spatial matching of the tracks of the incident beam and the hits on the 2S modules. This has provided the first measurements of the absolute efficiency of these prototype detectors.

Cluster efficiencies of approximately 99% and 98% have been measured for non-irradiated and
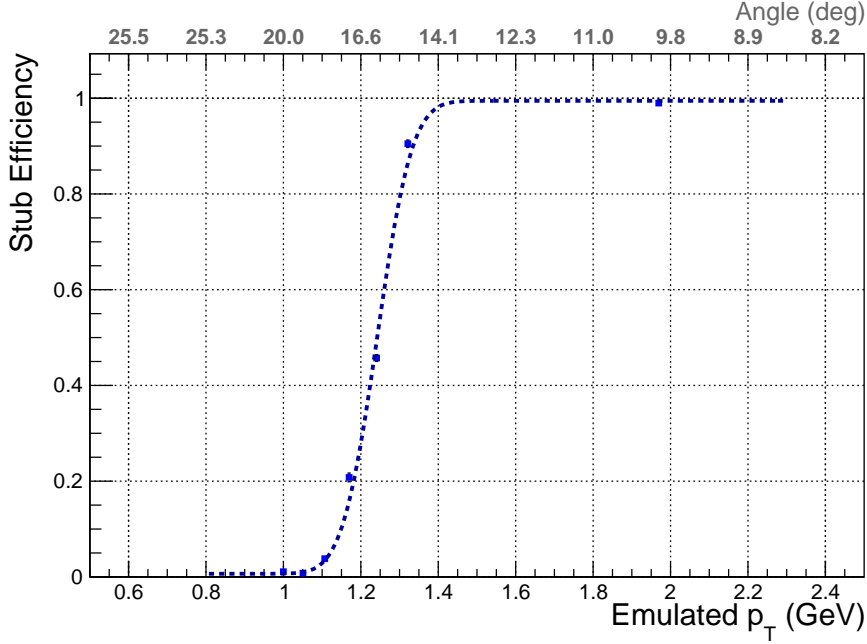
Figure 23: Stub efficiency of the full-size 2S module as a function of particle p_T measured at the Fermilab beam test facility during the angular scan. The module was operated at a bias voltage of $250\,V$ and the V_{CTH} value was set to 92. A radius of $60\,cm$ is used to convert the beam incident angle to effective p_T.

irradiated modules, respectively. These results are robust with respect to variations in particle arrival times relative to the trigger. For the non-irradiated module, an increase in the mean cluster width is observed as the beam incident angle increases. For the irradiated module, the average cluster size is higher in general and thus the variation of cluster width with angle is less evident.

The stub efficiency across all the strips of the sensors shows a uniform response. The stub efficiencies of both the non-irradiated mini-module and the full-size module are found to be around 99%. The stub efficiencies obtained from the analysis of data from the three test beam facilities are in agreement with each other. For the irradiated module, the stub efficiency was found to be 97%. All of the modules demonstrate the ability to reject tracks with $p_T < 2\,GeV$. The high efficiency of the irradiated module provides evidence that the modules will be able to operate throughout the lifetime of the HL-LHC without much loss of efficiency.

Acknowledgements

References

[1] CMS Collaboration, "The CMS experiment at the CERN LHC", 2008 *JINST* **3** S08004, `doi:10.1088/1748-0221/3/08/S08004`.

[2] CMS Collaboration, "Technical Proposal for the Phase-II Upgrade of the CMS Detector", Technical Report CERN-LHCC-2015-010, LHCC-P-008, CMS-TDR-15-02, 2015.

[3] CMS Collaboration, "The Phase-2 Upgrade of the CMS Tracker", Technical Report CERN-LHCC-2017-009, CMS-TDR-014, 2017.

[4] CMS Tracker Collaboration, "Test beam demonstration of silicon microstrip modules with transverse momentum discrimination for the future CMS tracking detector", 2018 *JINST* P03003, `doi:10.1088/1748-0221/13/03/P03003`.

[5] M. Raymond et al., "The CMS binary chip for microstrip tracker readout at the SLHC", *JINST* **7** (2012) C01033, `doi:10.1088/1748-0221/7/01/C01033`.

[6] W. Ferguson et al., "The CBC microstrip readout chip for CMS at the high luminosity LHC", *JINST* **7** (2012) C08006, `doi:10.1088/1748-0221/7/08/C08006`.

[7] D. Braga et al., "Characterization of the CBC2 readout ASIC for the CMS strip-tracker high-luminosity upgrade", 2014 *JINST* **9** C03001, `doi:10.1088/1748-0221/9/03/C03001`.

[8] G. Hall et al., "CBC2: A CMS microstrip readout ASIC with logic for track-trigger modules at HL-LHC", *Nucl. Instrum. Meth. A* **765** (2014) 214–218, `doi:10.1016/j.nima.2014.04.056`.

[9] D. Braga et al., "CBC2: a microstrip readout ASIC with coincidence logic for trigger primitives at HL-LHC", 2012 *JINST* **7** C10003, `doi:10.1088/1748-0221/7/10/c10003`.

[10] CMS Tracker Group Collaboration, "Service hybrids for the silicon strip modules of the CMS Phase-2 Outer Tracker upgrade", *PoS* **TWEPP2018** (2019) 127, `doi:10.22323/1.343.0127`.

[11] T. Gadek et al., "Front-end hybrids for the strip-strip modules of the CMS Outer Tracker Upgrade", *PoS* **TWEPP2018** (2019) 019, `doi:10.22323/1.343.0019`.

[12] "Irradiation Center Karlsruhe", `https://www.etp.kit.edu/english/irradiation_center.php`.

[13] H. Jansen et al., "Performance of the EUDET-type beam telescopes", *EPJ Techniques and Instrumentation* **3** (2016) 7, `doi:10.1140/epjti/s40485-016-0033-2`.

[14] C. Hu-Guo et al., "First reticle size MAPS with digital output and integrated zero suppression for the EUDET-JRA1 beam telescope", *Nucl. Instrum. Meth. A* **623** (2010) 480–482, `doi:10.1016/j.nima.2010.03.043`.

[15] T. Obermann et al., "Implementation of a configurable FE-I4 trigger plane for the AIDA telescope", 2016 *JINST* **9** C03035, `doi:10.1088/1748-0221/9/03/c03035`.

[16] D. Cussans, "A trigger/timing logic unit for ILC test-beams", CERN-2007-007 (2007).

[17] D. Cussans, "Description of the JRA1 Trigger Logic Unit (TLU), v0.2c", *EUDET-Memo-2009-4* (2009).

[18] V. Cerf and R. Kahn, "A protocol for packet network intercommunication", *IEEE Transactions on Communications* **22** (1974) 637–648, `doi:10.1109/TCOM.1974.1092259`.

[19] A. Bulgheroni, T. Klimkovich, P. Roloff, and A. Zarnecki, "EUTelescope: tracking software", Technical Report EUDET-Memo-2007-20, 2007.

[20] CMS Collaboration, "CMS Technical Design Report for the Pixel Detector Upgrade", Technical Report CMS-TDR-011, CERN-LHCC-2012-016, FERMILAB-DESIGN-2012-02, 2012. `doi:10.2172/1151650`.

[21] S. Kwan et al., "The pixel tracking telescope at the Fermilab Test Beam Facility", *Nucl. Instrum. Meth. A* **811** (2016) 162–169, `doi:10.1016/j.nima.2015.12.003`.

[22] P. Vichoudis et al., "The Gigabit Link Interface Board (GLIB), a flexible system for the evaluation and use of GBT-based optical links", 2010 *JINST* **5** C11007, `doi:10.1088/1748-0221/5/11/C11007`.

[23] C. G. Larrea et al., "IPbus: a flexible Ethernet-based control system for xTCA hardware", 2015 *JINST* **10** C02019, `doi:10.1088/1748-0221/10/02/C02019`.

[24] M. Kozlovszky, "A TCP/IP transport layer for the DAQ of the CMS experiment", *Nucl. Instrum. Meth. A* **534** (2004) 125, `doi:10.1016/j.nima.2004.07.076`.

[25] C. D. Jones, M. Paterno, J. Kowalkowski, L. Sexton-Kennedy, and W. Tanenbaum, "The New CMS Event Data Model and Framework", India:Macmillan, 2006. C06-02-13.

[26] M. Pesaresi et al., "The FC7 AMC for generic DAQ & control applications in CMS", 2015 *JINST* **10** C03036, `doi:10.1088/1748-0221/10/03/C03036`.

[27] G. Bauer et al., "The CMS event builder and storage system", *J. Phys. Conf. Ser.* **219** (2010) 022038, `doi:10.1088/1742-6596/219/2/022038`.

[28] CMS Collaboration, "CMS Computing: Technical Design Report", Technical Report CERN-LHCC-2005-023, CMS-TDR-7, 2005.

[29] C. Grandi et al., "CMS Computing Model: The "CMS Computing Model RTAG"", Technical Report CMS-NOTE-2004-031, CERN-LHCC-2004-035, LHCC-G-083, CERN, 2004.

[30] R. Brun and F. Rademakers, "ROOT: An object oriented data analysis framework", *Nucl. Instrum. Meth. A* **389** (1997) 81–86, `doi:10.1016/S0168-9002(97)00048-X`.

[31] V. Blobel, "Software alignment for tracking detectors", *Nucl. Instrum. Meth. A* **566** (2006) 5 – 13, `doi:10.1016/j.nima.2006.05.157`. 2005.

[32] K. Rose, "Deterministic annealing for clustering, compression, classification, regression, and related optimization problems", *IEEE Proc.* **86** (1998) 2210–2239, `doi:10.1109/5.726788`.

[33] F. Didierjean, G. Duchene, and A. Lopez-Martens, "The Deterministic Annealing Filter: A new clustering method for γ-ray tracking algorithms", *Nucl. Instrum. Meth. A* **615** (2010) 188–200, `doi:10.1016/j.nima.2010.01.030`.

[34] C. Kleinwort, "General broken lines as advanced track fitting method", *Nucl. Instrum. Meth. A* **673** (2012) 107 – 110, `doi:10.1016/j.nima.2012.01.024`.